LDV measurements of Newtonian and non-Newtonian open-surface swirling flow in a hydrodynamic mixer

Péter Csizmadia, *Csaba* Hős

Abstract

The aim of this paper is to study the cyclone-like flow inside a hydrodynamic mixer experimentally, with a special emphasis on the differences in the flow field in the case of Newtonian and non-Newtonian fluids. The mixer consists a cylindrical body with conical bottom, in which two, tangentially entering fluid jets drive the rotating motion of the fluid body. The two fluids are (1) water and (2) a Carbopol solution obeying power-law rheology. The circumferential and axial velocity distributions were measured with the help of LDV for several fluid levels and driving flow rates. We show that in the case of water, the velocity distributions are qualitatively similar for several flow rates if the fluid height is kept constant. In the case of the power-law fluid, the measured velocity profiles show less generality.

Keywords

Carbopol solution · hydrodynamic mixer · LDV measurements · non-Newtonian rheology · highly swirling flow

Péter Csizmadia

Budapest University of Technology and Economics, Department of Hydrodynamic Systems (HDS), H-1111, Budapest, Bertalan Lajos u 7, Hungary
e-mail: csizmadia@hds.bme.hu

Csaba Hős

Budapest Univerisity of Technology and Economics, Department of Hydrodynamic Systems (HDS), H-1111, Budapest, Bertalan Lajos u 7, Hungary
e-mail: csaba.hos@hds.bme.hu

1 Introduction

1.1 Motivation

This paper presents the results of a measurement series studying the flow field inside a hydrodynamic mixer with the help of LDV measurements. The actual industrial application is a dense slurry mixer which is used in coal-fired power plants where the dry bed ash and the water are mixed and the mixture is pumped to the deposition site. Computational Fluid Dynamics (CFD) techniques play a central role in the improvement of these mixers, but experimental results are also extremely important to validate the CFD approach. Thus, a scaled-down mixer was built with Plexiglas walls allowing visual access to the flow for the LDV system. The original fluid (slurry) is a non-Newtonian material which is not suitable for the LDV measurements because of visual problems. Hence another non-Newtonian fluid — Carbopol solution — was chosen which allows visual access up to a limited radial depth (see section 2.1 for details).

Due to the highly swirling flow field inside the mixer, capturing the velocity profiles by CFD is a challenging task, not to mention the additional complexity due to the non-Newtonian fluid. Hence, the results of the current study are intended to serve as validation cases for the CFD simulation of both Newtonian and non-Newtonian fluids. Moreover, the presented results also contribute to the understanding of the flow field inside such mixers, which are designed nowadays mostly based on anecdotal rules of thumbs and on-site experiences.

1.2 Literature overview

Several researchers deal with the determination of the flow field inside hydrocyclones which are used not only for separating solid contamination (particles of different sizes) but also for mixing purposes (e.g. static mixers). Some studies apply numerical methods, for instance [6], in which the authors compare three turbulence models and they employ their results for improving the geometry of the hydrocyclones in [7]. Other studies concentrate on predicting separation efficiency by means of CFD technique (e.g. [11]) and predicting the effect of varying geometries (e.g.: [12]). [14] studies a water and diesel fuel separator numerically for several geometries in which the separation

efficiency can improve. In [8], solid-liquid suspension was investigated with the CFD technique and their results show a fairly good agreement with the literature. In [1] solid-liquid separation processes were tested experimentally. [15] applies both numerical and experimental techniques for studying the separation inside a hydrocyclone. In [3] four different turbulence models were tested and compared against experimental results and the best agreement was found using the RMS model. Further studies in this field can be found in [4].

2 Experimental set-up

2.1 Rheological properties

Newtonian (water) and non-Newtonian (Carbopol solution) fluids were used to highlight the difference in the velocity distribution. Corresponding to the non-Newtonian fluid, the Carbopol solution consisted of 0.13m/m% Carbopol 971 powder, 0.05m/m% NaOH (to set the pH-value to approximately 7), and 99.82m/m% water. The rheological measurements were performed with the help of Rheotest RV2 rotational viscometer, before every modification of the fluid level or vertical position (see Section 3 for details). The rheological measurements show that the Carbopol solution behaves as a power-law fluid which can be described by

$$\tau = \mu \dot{\gamma}^n, \tag{1}$$

with μ[Pas^n] consistency index and n[−] flow behavior index (for details see [9]). During the measurements lasting for approx. 15 days we experienced a decrease in the shear stress τ for a given strain rate $\dot{\gamma}$ which is most likely caused by the destructive effect of the impeller of the driving radial pump. Thus the rheology curves were measured before each measurement campaign. By denoting the cumulative measurement hours by MH and applying simple curve fit we found that at $\dot{\gamma}_{max} = 1312/s$ we have

$$\tau_{max} = 0.0152 - 0.6155\,MH + 33.267\,MH^2. \tag{2}$$

The above equation describes the measured $\tau_{max}(MH)$ relationship with $R^2 = 0.91$ coefficient of determination. By taking the average value of the consistency index $\overline{\mu} = 0.3532$Pas^n, the actual rheology curve of the solution after MH measurement hours can be given by

$$\tau = \overline{\mu}\dot{\gamma}^n, \quad \text{with} \quad n = \frac{\lg \tau_{max}(MH) - \lg \overline{\mu}}{\lg \dot{\gamma}_{max}}. \tag{3}$$

For example, we have $n(0) = 0.633$ and $n(20) = 0.604$, i.e. 4.58% decrease in 20 hours of measurement. In what follows, we always indicate the actual measurement hours (MH) corresponding to the actual figure. Thus, making use of (2) and (3), one can find the actual rheology curve.

2.2 The mixer and the LDV system

Fig. 1 and 2 present the photo and the sketch of the scaled-down mixer. In the mixer (5) the fluid motion is driven by two
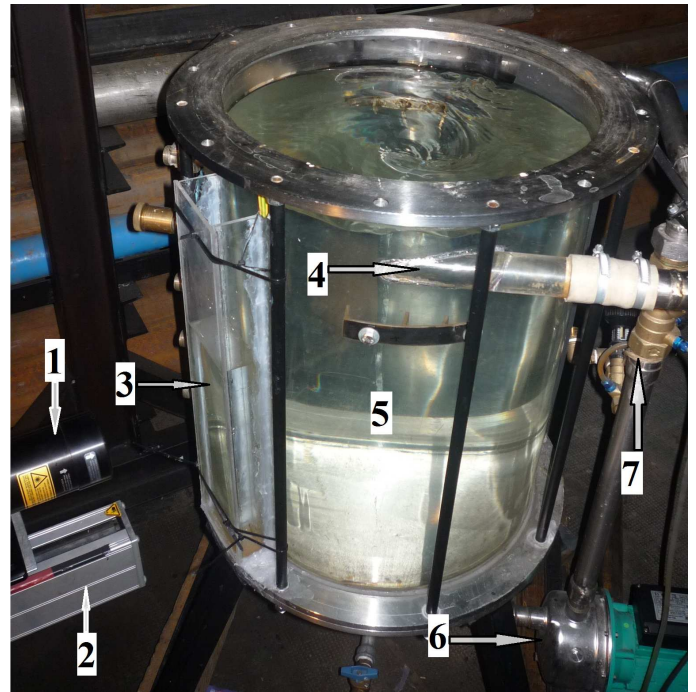
Fig. 1. The experimental scaled-down mixer.
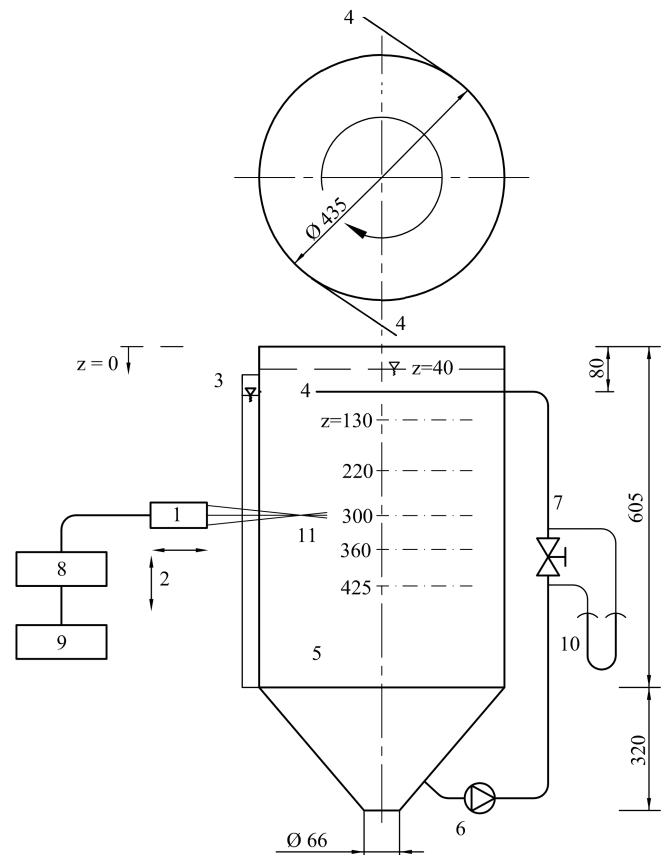
Fig. 2. The sketch of the scaled-down mixer, the main dimensions are in millimeter.
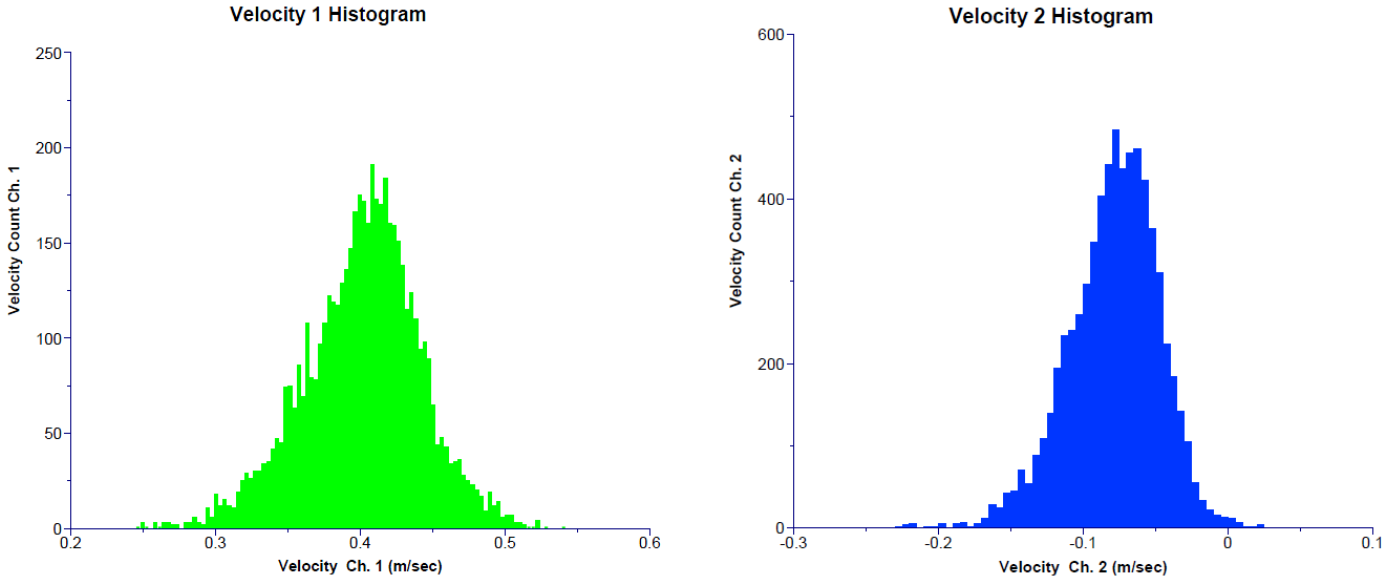
Fig. 3. Typical circumferential (left) and axial (right) velocity histograms.

tangential jets (4) fed by a centrifugal pump (6). A control valve (7) is mounted to set and measure the recirculated flow rate with the help of the pressure taps measuring the pressure drop on the valve. This pressure difference was calibrated separately to provide the desired $\Delta p(Q)$ relationship which allows the quick setting of the flow rate based on the U-tube manometer (10).

The axial and circumferential velocity components were measured by the two-component TSI TLN06-363 LDV system (1) which was positioned by a traverse system (2) in three dimensions, with an accuracy of 0.1 mm. Moreover, the LDV system consists of a data acquisition system (depicted by 8 in Fig. 2) which transfers the data to the PC (9). To reach better accuracy at each measuring point 10000 bursts were collected, with a timeout (the maximum time interval of sampling) of 300 seconds. Fig. 3 depicts typical measured velocity histograms.

To minimize the spatial error caused by the refraction due to the 6 mm thick and curved Plexiglas wall, an additional tank with 5 mm thick and planar walls (3) was mounted to the mixer and filled with water. This extra element minimized the effect of the curved tank wall and allowed a maximal "insight" up to $r = 116$ mm (i.e. $r/R \approx 0.4$), where r is the radial coordinate measured from the axis and R is the radius of the mixer. In what follows, we show the velocity distributions mostly in the $0.4 < r/R < 1$ (figs. 4 - 6) and $0.7 < r/R < 1$ (fig. 7) region. The spatial shift caused by the different refraction indexes of the materials is also considered with the analytical formulae of classic optics [13]. The measurements were performed on a radial grid of $\Delta r = 0.5$ mm close to the wall and $\Delta r = 2$ and $\Delta r = 5$ mm in the inner regions. The standard deviation of the data was 5-20 %, the higher values corresponding to the region close to the wall and lower ones to the inner regions. This deviation includes all the influencing effects, e.g. unsteadiness of the feed flow rate, splashing near the free surfaces, secondary precessing motion of the fluid body or the accuracy of the LDV system. Ac-

tually, according to the manufacturer, the measurement accuracy of the LDV system is 2%.

As seeding for the LDV experiments, polymer spheres of diameter 50-100 μm were used (Spheriglass). To show that this type of tracers is adequate for our purposes (especially in the case of non-Newtonian fluid) we adapt the approach of Bewley *at al.* described in [2]. Without giving here the detailed train of thought, the main result in [2] is that if the constant

$$B = \left[\frac{\rho_f^3}{\rho_p \Delta \rho^2}\right]^{\frac{2}{3}} \left[\frac{v^2}{gd^3}\right]^{\frac{4}{3}} \tag{4}$$

is larger than one, the tracer particles are suitable for the measurement. In (4) ρ_f, ρ_p, and $\Delta \rho$ are the fluid, particle densities and the density difference, respectively. v is the fluid kinematic viscosity and d is the tracer diameter. In our case the tracer density is 1100kg/m^3 while the fluid density is 1000kg/m^3 for both cases (Newtonian and non-Newtonian fluid). The kinematic viscosities are $v = 10^{-6} \text{m}^2/\text{s}$ (water) and $v = 353.2 \times 10^{-6} \text{m}^2/\text{s}$ for the Carbopol solution (average value, see next section for details). With these values, we obtain $B = 963$ for water and $B = 6 \times 10^9$ for the Carbopol solution.

We also computed the timescale associated with the tracer particles (see [2]) for details:

$$\tau_p = \frac{\rho_p d^2}{18\mu}, \tag{5}$$

which turns out to be $\tau_p = 0.61$ms for water and $\tau_p = 0.0017$ms for the Carbopol solution. The highest measured fluid velocity was $v_{max} \approx 0.6$m/s, which gives $\tau_f = D_{tank}\pi/v_{max} = 2.17$s for the timescale of the fluid motion. The three orders of magnitude difference between the particle and the fluid motion timescale also confirms the suitability of the choice of tracer particles.

The temperature of the fluid varied in the range of $19\,°C$ to $27\,°C$. We were unable to find any data on how the refractive

index of the Carbopol solution changes in this regime, however, [10] performs detailed light scattering measurements investigating Carbopol ETD2050 dispersed in water without any direct temperature control. Rheological measurements in this temperature range showed no significant variation in the material properties. Note that [4] contains a more detailed description of the experimental set-up, especially the LDV system.

3 Results

3.1 Newtonian fluid: water

3.1.1 Fully filled tank

Fig. 4 shows the results of the measurements in the case of Newtonian fluid (water) and fully filled tank (water level: $z = 40$, see Fig. 2 for details). We chose the inlet jet velocity to non-dimensionalize the circumferential velocity component, which is depicted in the left column while the axial ones are shown in the right column. Three vertical positions were chosen to measure the velocity components: $z = 130$, 220, and 425 mm. The effect of the jets (high-velocity layer) can be seen near the wall of the mixer which is clearer in the upper region (e.g. $z = 130$ mm) and less visible in the deeper regions (e.g. $z=425$), similar effect was reported in [5]. Away from the wall ($r/R < 0.75$) a hyperbolic ($1/r$-like) velocity profile can be observed which is due to the presence of a free vortex [9], a velocity distribution characteristic of cyclone-like flows, see e.g. [6] and [11].

In the case of the axial velocity component (right column of Fig. 4), the reference velocity is $v_{ref} = Q/A_{tank}$, where the Q is the flow rate entering in the two jets and A_{tank} is the area of the cylindrical tank. These velocity values are approximately one order of magnitude smaller than the tangential ones, as highlighted in Tab. 1. Fig. 4 suggests that close to the wall ($r/R > \approx 0.85$), the fluid moves downwards which is more expressive in the upper region (e.g. $z = 130$ mm) and less significant in the deeper region (e.g. $z = 425$ mm). Closer to the centreline ($0.4 < r/R < 0.85$), an upwards motion can be observed similar to the observations of [6], [11], and [3].

It is interesting to observe that the dimensionless form of both dimensionless velocity components coincide for different driving flow rates. The maximum deviation between the dimensionless velocity values are less than 10 % in this fluid level, except the values which are close to zero and in the case of the uppermost axial component ($z=130$ mm), close to the wall, where we observe high uncertainty in the profiles. The origin of this uncertainty (upper right panel in Fig. 4) is not definitely known; we observed velocity histograms with two peaks; one of them being zero while the other one is a small, wide-spread peak with non-zero mean. We consider this close-wall data as measurement error.

In this case (fully filled tank with water), single-phase CFD pre-computations are available in [4] in which a fairly good agreement can be observed between the measured and simulated values. The near-wall measurement uncertainty mentioned

Tab. 1. Flow rates and reference velocities.

	Q_{max}	Q_{mid}	Q_{min}
Q, liter/min	76.5	48.7	33.2
v_{jet}, m/s	8.11	5.16	3.52
v_{ref}, m/s	0.0086	0.0055	0.0037

above (upper right panel in Fig. 4) was not experienced in these measurements.

3.1.2 Semi-filled tank

Fig. 5 presents the results of the measurements in the case of semi-filled tank (fluid level: $z = 305$mm) with the above mentioned (sec. 3.1.1) dimensionless form. The axial positions of the measurements are $z = 360$, 400, 425mm. The most significant difference from the fully filled tank case (see Fig. 4) is that in the case of the circumferential components (left column) the deviation is between 30-50 %. However, the velocity profiles are still qualitatively similar suggesting that another velocity scaling that corrects the discrepancy should be possible. The above mentioned (sec. 3.1.1) dimensionless axial velocity components are also qualitatively similar, except for the region closer to the wall. However, the cause of this discrepancy is easy to reveal: at different flow rates the jets impact the rotating fluid body at different circumferential locations. As the measurement location is fixed, the upward and downward motion heavily depends on the relative circumferential location and on the measurement line.

During the measurements, relatively intensive splashing on the fluid surface was experienced. In the case of the half-filled tank the deviations of the velocity components from the mean value were higher than for the fully filled tank. However, this deviation does not decrease significantly in the deeper regions (i.e. far away from the surface). The fluctuation seems related more to the relative circumferential location of the impinging fluid jet and measurement line. In other words, the impact of the fluid jet and the rotating fluid body results in a more profound excitation than the splashing on the surface. Moreover, in the inner region a precessing motion can be formed that also leads to the velocity fluctuations.

3.2 Non-Newtonian fluid: Carbopol solution

3.2.1 Results in the case of higher fluid levels

Fig. 6 presents the velocity distributions in the case of the Carbopol solution with the reference velocities defined in Section 3.1.1. These measurements were performed with the maximal flow rate given in Tab. 1, with three different fluid levels ($z=40$, 95 and 205 mm), and at three axial positions ($z=300$, 360, and 425 mm). Similar to the previous plots, the left column includes the circumferential velocity components. The first thing we notice is that the velocity scaling does not result in identical velocity profiles. In the case of the maximum fluid level ($z=40$ mm), the peak tangential velocity is lower because the fluid level above the measurement height disperses the im-
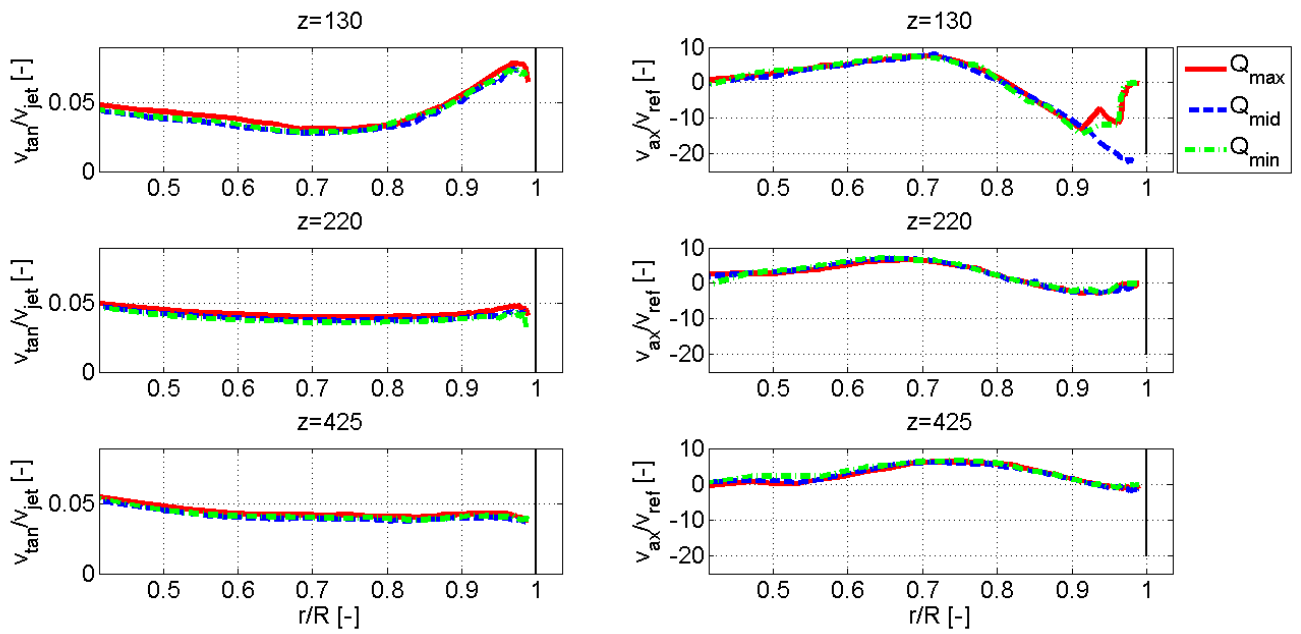
Fig. 4. Dimensionless circumferential (left) and axial (right) velocity distributions at Q_{max} (solid lines), Q_{mid} (dashed lines), and Q_{min} (dash-dot lines) in the case of water and fully filled tank (water level: $z = 40$mm).
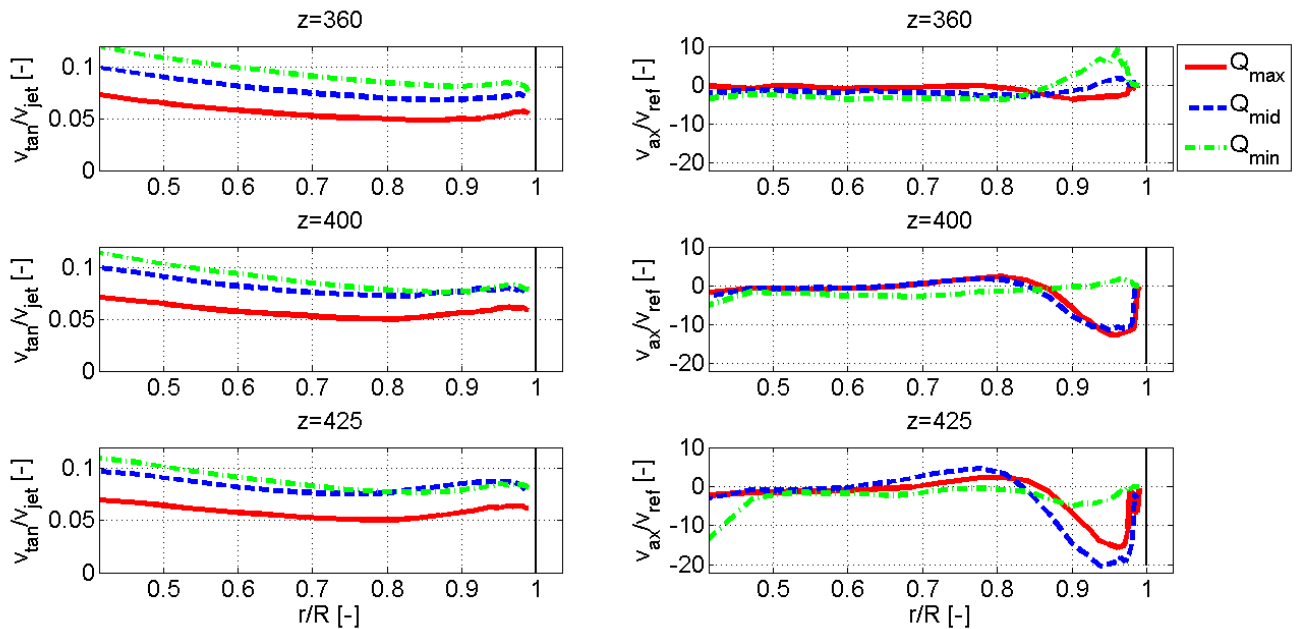
Fig. 5. Dimensionless circumferential (left) and axial (right) velocity distributions with Q_{max} (solid lines), Q_{mid} (dashed lines), and Q_{min} (dash-dot lines) in the case of water and semi-field tank (water level: $z = 305$mm).
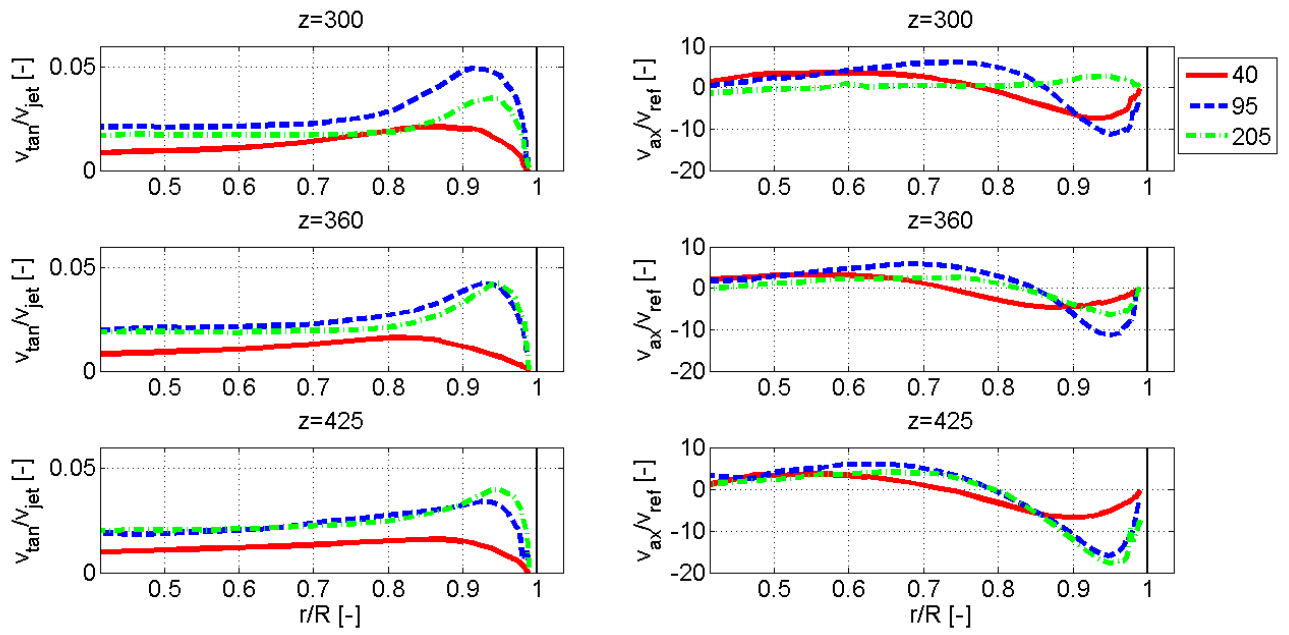
Fig. 6. Dimensionless circumferential (left) and axial (right) velocity distributions with different fluid levels: z=40 mm, MH=7.4-9.25 (solid lines), z=95 mm, MH=10.48-12.33 (dashed lines), and z=205 mm, MH=12.95-14.8 (dash-dot lines) in the case of Carbopol solution.
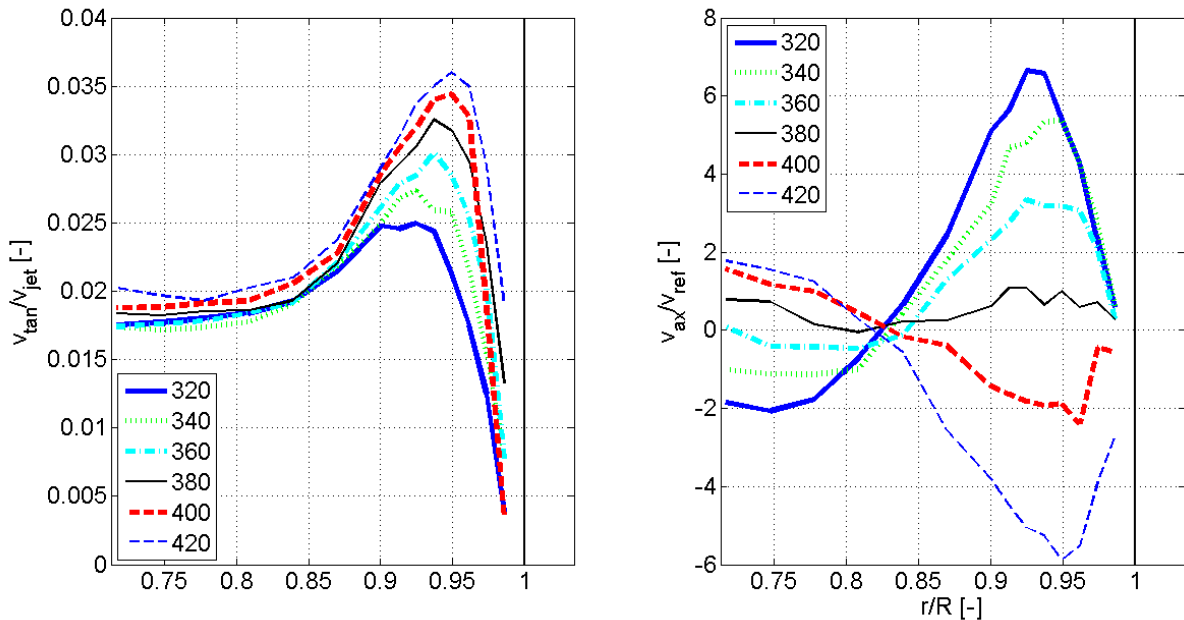
Fig. 7. Dimensionless circumferential (a,) and axial (b,) velocity distributions in a lower fluid level (z=255 mm, MH=14.8-16.52) in six, different axial positions in the case of Carbopol solution.

pulse of the jet. (This phenomena was not observed in the case of water as its viscosity is 300 times smaller; hence internal dissipation is much weaker.) Upon reducing the level of the fluid, this loss decreases but the fluid friction between the jets and the wall of the mixer increase. Moreover the degree of the impact of the jet also rises. The differences decrease while moving to the centreline. We also note that the hyperbolic profile mentioned in section 3.1.1 cannot be observed in the $0.4<r/R<0.8$ range, although we have no information on the innermost ($r/R < 0.4$) range.

The axial velocity components (right column) shows a downward motion close to the wall, which is consistent with the results of the water (see previous section). If the fluid level reduces ($z=205$ mm), the above mentioned (section: 3.1.2) effect (dependence of the profiles on the relative circumferential location of the jet impact and the measurement) also appears (see the $z=300$ mm axial position), consequently, the velocity distribution is a function of the circumferential position. Moving to the centreline, the differences between the axial velocity components decrease.

3.2.2 Results in the case of lower fluid level

Fig. 7 shows the velocity distributions in the case of Carbopol solution, in the case of lower fluid level ($z = 255$ mm) and at six axial positions ($z = 320, 340, ..., 420$ mm). It can be seen that the dimensionless circumferential velocity components (left panel of Fig. 7) increase while moving to the bottom region which means that the impact of the jet to the rotated fluid occurred at an earlier circumferential position, therefore the "main stream" can be found in this (lower) section of the fluid. This can be also seen on the axial velocity components (right panel of Fig. 7 b,), because the downward motion can be observed at the lower positions ($z = 400, 420$ mm). Close to the fluid surface, the upward motion dominates. Note the different scale on the x axis.

4 Conclusion

In this paper, the axial and circumferential velocity distributions were studied experimentally inside a hydrodynamic mixer. In the case of water we introduced a scaling, with which the dimensionless velocity profiles coincide in the case of fully filled tank but show only qualitative agreement for semi-filled tank. With respect to the circumferential velocity components, the effect of the jets can be observed close to the wall and the hyperbolic velocity profile appears moving to the centreline. In the case of axial velocity components, the downward motion dominates close to the wall and insignificant upward motion can be observed the inner region, see e.g. [5]. With respect to the Carbopol solution, only qualitative agreement can be seen with the results of water, but the hyperbolic velocity profile can not be found in this range ($r/R>0.4$). The importance of the circumferential position are based on the result of both examined fluids. The presented results can be used as validation for future numerical simulations.

References

1 **Ahmed MM, Ibrahim GA, Farghaly MG**, *Performance of a three-product hydrocyclone*, International Journal of Mineral Processing, **91**(1-2), (2009), 34–40, DOI 10.1016/j.minpro.2008.11.005.

2 **Bewley GP, Sreenivasan K, Lathrop D P**, *Particles for tracing turbulent liquid helium*, Experiments in Fluids, **44**(6), (2008), 887–896, DOI 10.1007/s00348-007-0444-6.

3 **Bhaskar K, Murthy Y, Raju M, Tiwari S, Srivastava J, Ramakrishnan N**, *CFD simulation and experimental validation studies on hydrocyclone*, Minerals Engineering, **20**(1), (2007), 60–71, DOI 10.1016/j.mineng.2006.04.012.

4 **Csizmadia P, Hős Cs, Pandula Z**, *LDV Measurements and CFD Simulations of the Swirling Flow in a Hydrodynamic Mixer*, Proceedings of Conference on Modelling Fluid Flow (CMFF'12), **2**, (2012), 545–551.

5 **Dai GQ, Li J, Chen W**, *Numerical prediction of the liquid flow within a hydrocyclone*, Chemical Engineering Journal, **74**(3), (1999), 217–223, DOI 10.1016/S1385-8947(99)00044-3.

6 **Delgadillo JA, Rajamani RK**, *Exploration of hydrocyclone designs using computational fluid dynamics*, International Journal of Mineral Processing, **84**(14), (2007), 252–261, DOI 10.1016/j.minpro.2006.07.014.

7 **Delgadillo JA, Rajamani RK**, *A comparative study of three turbulence-closure models for the hydrocyclone problem*, International Journal of Mineral Processing, **77**(4), (2005), 217–230, DOI 10.1016/j.minpro.2005.06.007.

8 **Ghasemi N, Sohrabi M, Khosravi M, Mujumdar AS, Goodarzi M**, *CFD simulation of solid-liquid flow in a two impinging streams cyclone reactor: Prediction of mean residence time and holdup of solid particles*, Chemical Engineering and Processing: Process Intensification, **49**(12), (2010), 1277–1283, DOI 10.1016/j.cep.2010.09.016.

9 **Lajos T**, *Basics of fluid mechanics*, Műegyetem Kiadó, 2008.

10 **David Lee**, *Structural Investigation of Carbopol ETD2050 by Light Scattering*, Dept. of Physics, Simon Fraser University, 2009.

11 **Mainza A, Narasimha M, Powell M, Holtham P, Brennan M**, *Study of flow behaviour in a three-product cyclone using computational fluid dynamics*, Minerals Engineering, **19**(10), (2006), 1048–1058, DOI 10.1016/j.mineng.2006.03.014.

12 **Raoufi A, Shams M, Farzaneh M, Ebrahimi R**, *Numerical simulation and optimization of fluid flow in cyclone vortex finder*, Chemical Engineering and Processing: Process Intensification, **47**(1), (2008), 128–137, DOI 10.1016/j.cep.2007.08.004.

13 **Ruck B**, *Laser-Doppler-Anemometrie*, AT-Fachverlag GmbH, Stuttgart, 1987.

14 **Schütz S, Gorbach G, Piesche M**, *Modeling fluid behavior and droplet interactions during liquid-liquid separation in hydrocyclones*, Chemical Engineering Science, **64**(18), (2009), 3935–3952, DOI 10.1016/j.ces.2009.04.046.

15 **Sripriya R, Kaulaskar M, Chakraborty S, Meikap B**, *Studies on the performance of a hydrocyclone and modeling for flow characterization in presence and absence of air core*, Chemical Engineering Science, **62**(22), (2007), 6391–6402, DOI 10.1016/j.ces.2007.07.046.